

## Two-dimensional electrostatic lattices for indirect excitons

M. Remeika,<sup>1,a)</sup> M. M. Fogler,<sup>1</sup> L. V. Butov,<sup>1</sup> M. Hanson,<sup>2</sup> and A. C. Gossard<sup>2</sup>

<sup>1</sup>Department of Physics, University of California at San Diego, La Jolla, California 92093-0319, USA

<sup>2</sup>Materials Department, University of California at Santa Barbara, Santa Barbara, California 93106-5050, USA

(Received 29 September 2011; accepted 4 January 2012; published online 6 February 2012)

We report on a method for the realization of two-dimensional electrostatic lattices for excitons using patterned interdigitated electrodes. Lattice structure is set by the electrode pattern and depth of the lattice potential is controlled by applied voltages. We demonstrate square, hexagonal, and honeycomb lattices created by this method. © 2012 American Institute of Physics.  
[doi:10.1063/1.3682302]

Studies of particles in periodic potentials are fundamental to condensed matter physics. While originally experimental studies concerned electrons in crystal lattices, a variety of systems with particles in artificial lattice potentials are actively investigated at present. Controlling the parameters of an artificial lattice provides a tool for studying the properties of particles confined to the lattice and, to some extent, for emulating condensed matter systems. Cold atoms in an optical lattice present a prominent example of particles in artificial lattices. Phenomena originally considered in context of condensed matter systems, such as the Mott insulator–superfluid transition, can be studied in the system of cold atoms in optical lattices.<sup>1</sup>

Excitons in artificial lattices present a condensed matter system of particles in periodic potentials.<sup>2–10</sup> In particular, artificial periodic potentials, both static and moving, can be created for indirect excitons.<sup>2,3,6,10</sup> An indirect exciton in coupled quantum wells (CQW) is a bound state of an electron and a hole in separate QWs (Fig. 1(a)). Due to a dipole moment of indirect excitons  $ed$  ( $d$  is close to the distance between the QW centers), potential landscapes for excitons  $E(x,y) = edF_z(x,y) \propto V(x,y)$  can be created using a laterally modulated gate voltage  $V(x,y)$  ( $F_z$  is the  $z$ -component of electric field in the CQW layers).<sup>2,3,6,10–18</sup> Furthermore, due to their long lifetimes, orders of magnitude longer than that of regular excitons, indirect excitons can travel in electrostatically created potentials over large distances before recombination.<sup>6,10,11,13,15–18</sup> Also, due to their long lifetimes, these bosonic particles can cool to temperatures well below the temperature of quantum degeneracy.<sup>19</sup> Therefore, the system of indirect excitons in electrostatic lattices gives an opportunity to study transport of cold bosons in periodic potentials.

Lattice potentials with energy modulation in one dimension were created for indirect excitons by interdigitated gates.<sup>2,6,10</sup> However, a number of phenomena, including the Mott insulator–superfluid transition, require in-plane energy modulation in both dimensions.<sup>1</sup> A two-dimensional (2D) lattice for excitons can be generated by a single electrode with a periodic array of holes.<sup>3</sup> The lateral modulation of  $F_z$ , which determines the lattice depth, can be controlled by

changing the voltage applied to the electrode. However, within this method, changing the lattice amplitude is accompanied by changing the average electric field  $F_z^{avg}$  and, in turn, lifetime and density of indirect excitons. An independent control  $F_z^{avg}$  and the lateral modulation of  $F_z$  can be realized using multiple electrodes separated by insulating layer(s).<sup>20</sup> However, within this method, a considerable fraction of the applied voltage may drop in the deposited insulator. This fraction and, in turn,  $F_z(x,y)$  may depend on the optical excitation.

Here, we present a method for creating 2D electrostatic lattices for indirect excitons that utilizes variable electrode density.<sup>21</sup> We demonstrate that 2D lattices for excitons can be produced by patterned interdigitated gates. The lattice constant and lattice structure are determined by the electrode pattern. Figures 1(c)–1(e) show the electrode patterns for creating square, triangular, and honeycomb lattices, respectively. The corresponding simulated exciton potential profiles are shown in Figs. 1(f)–1(h). The average field  $F_z^{avg}$  and spatial modulation of  $F_z$  can be independently controlled by voltages  $V_0$  and  $\Delta V$ .  $F_z^{avg}$  realizes the indirect exciton regime and controls the exciton lifetime. Modulation of  $F_z$  forms the lattice potential (Fig. 1(b)). The lattice amplitude can be controlled *in situ* by  $\Delta V$ . The in-plane electric field in the lattice  $F_{xy}$  is small so that it does not cause the exciton dissociation:  $eF_{xy}a_B \ll E_{ex}$ ,  $a_B \sim 20$  nm and  $E_{ex} \sim 4$  meV are the Bohr radius and binding energy for the indirect excitons, respectively.<sup>22,23</sup> (Fig. 1(b)).

Advantages of this method include (i) a variety of 2D lattice structures for excitons can be realized; (ii) the depth of the lattice potential can be controlled *in situ* by voltage; (iii) the average field can be controlled by voltage independently from lattice depth; (iv) smooth 2D lattice potentials are realized by the electrode patterns; and (v) the lattice device can be fabricated using single layer lithography with no deposited insulator layer.

We demonstrate experimental proof of principle for creating 2D lattices for excitons by this method. A square lattice potential (Fig. 1(f)) is used for the demonstration. CQW structure is grown by MBE. A  $n^+$ -GaAs layer with  $n_{Si} = 10^{18}$  cm<sup>-3</sup> serves as a homogeneous bottom electrode. Semitransparent top patterned electrodes are fabricated by evaporating 2 nm Ti and 7 nm Pt. CQW with 8 nm GaAs QWs separated by a 4 nm Al<sub>0.33</sub>Ga<sub>0.67</sub>As barrier are

<sup>a)</sup>Author to whom correspondence should be addressed. Electronic mail: remeika@physics.ucsd.edu.

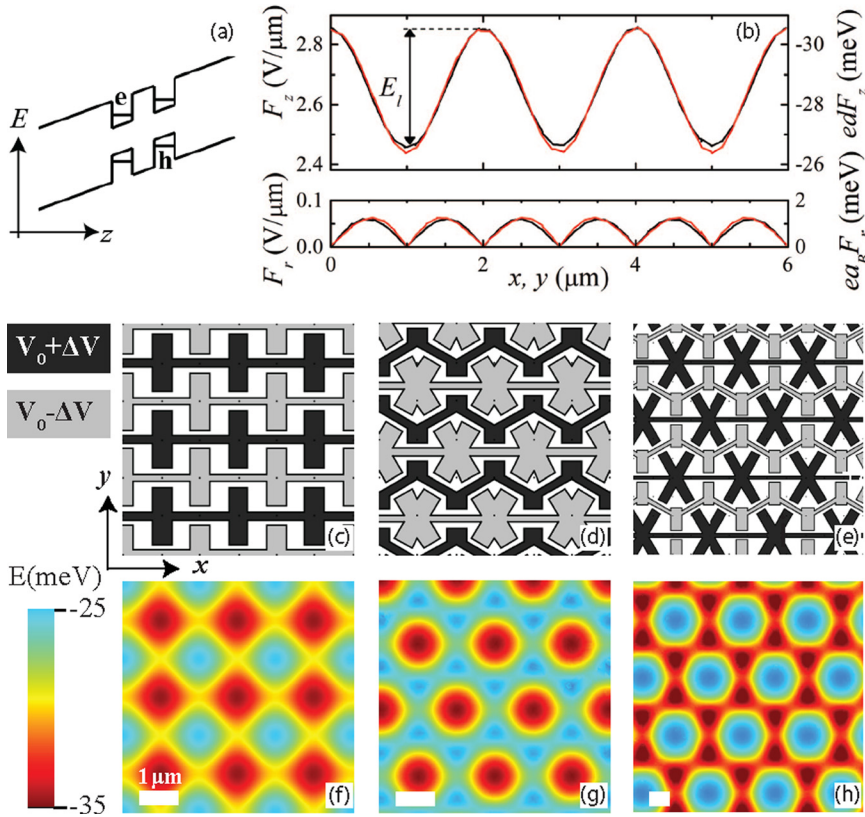


FIG. 1. (Color online) (a) Energy diagram of the CQW. (b) Simulated electric field  $F_z$  and exciton energy  $edF_z$  along  $x$  (black) and  $y$  (red, gray in print) for square lattice. Lower plot shows lateral electric field  $F_r = (F_x^2 + F_y^2)^{1/2}$  and  $eF_r$ . (c)–(e) Electrode schematics for square, triangular, and honeycomb lattices, respectively. (f)–(h) Simulated exciton energy for these electrode patterns.  $\Delta V = 1$  V.

positioned 100 nm above the  $n^+$ -GaAs layer within an undoped  $1\ \mu\text{m}$  thick  $\text{Al}_{0.33}\text{Ga}_{0.67}\text{As}$  layer. Excitons are photogenerated by a Ti:Sapphire laser tuned to the energy of direct excitons in this sample ( $\approx 786$  nm). Exciton density is controlled by the laser excitation power  $P_{ex}$ . Photoluminescence (PL) images of the exciton cloud are captured by a CCD with a filter selecting photon wavelengths  $\lambda = 800 \pm 5$  nm covering the spectral range of the indirect excitons. The spectra are measured using a spectrometer with resolution  $0.18$  meV. Experiments are done at  $T_{\text{bath}} = 1.6$  K.

Figures 2(a)–2(d) show the emission profiles for excitons in a square lattice along  $x$  or  $y$ . Each point in the  $x$ -profiles is obtained by averaging over 5 lattice sites along  $y$  and *vice versa* to reduce the noise in the data. Another source of averaging is finite optical resolution, see below (note that averaging reduced the amplitude of the spatial modulations discussed below). The quantity  $\hbar\omega$  in Figs. 2(b) and 2(d) stands for the spectral average  $\hbar\omega = M_1/I$ , where  $I = \int I_{\omega'} d\omega'$  is the total PL intensity and  $M_1 = \int I_{\omega'} \hbar\omega' d\omega'$  is its first spectral moment. As one can see in Fig. 2, both  $I$  and  $\hbar\omega$  are modulated with the period matching the lattice constant revealing the exciton confinement in the 2D lattice. The intensity maxima match the energy minima demonstrating exciton collection in the lattice sites.

We also probe exciton transport in the lattice. Figures 2(e)–2(g) show spatial images of exciton PL at three different lattice depths. As the lattice depth is turned up the exciton cloud width becomes smaller and locations of the lattice sites become apparent in the PL image. Figure 2(h) shows the full width at half maximum (FWHM) of the exciton cloud PL as a function of  $P_{ex}$  for lattice depths  $E_l = 0$  and  $4.2$  meV. At low exciton densities, the emission spot is

essentially equal in size to the laser excitation spot indicating that excitons are localized and do not travel outside the laser excitation spot. At high exciton densities, the emission spot is larger than the laser excitation spot indicating that excitons are delocalized and travel outside the laser excitation spot (Fig. 2(h)). In similarity to the localization-delocalization transition studied in linear lattices,<sup>6</sup> this behavior corresponds to the exciton localization in the combined lattice potential and disorder potential at low densities and exciton delocalization due to screening of the potential by the repulsively interacting excitons (the amplitude of the disorder potential in the sample is  $\sim 0.6$  meV). Figure 2(h) shows that a higher exciton density and, in turn, higher interaction energy is required for screening the potential with a higher lattice amplitude, in agreement with this model.

In order to examine this agreement quantitatively, we considered a mean-field model<sup>6</sup> where the local density  $n(\mathbf{r})$  of bright excitons is the solution of the equation

$$\varepsilon(n) \equiv T \ln(1 - e^{n/2\nu_1 T}) = E(\mathbf{r}) + \frac{\gamma}{\nu_1} n - \zeta. \quad (1)$$

Here  $\nu_1 = m/(2\pi\hbar^2)$  is the density of states per spin,  $\gamma$  is the dimensionless interaction constant,  $\zeta$  is the exciton electrochemical potential, and  $T$  is the exciton temperature. Within this model, the first moment of the exciton emission energy proves to be

$$M_1 = (\zeta - \varepsilon)n + 2\nu_1 T^2 \text{Li}_2(e^{\varepsilon/T}), \quad (2)$$

where  $\text{Li}_2(z)$  is the dilogarithm function. From these two quantities, the local PL intensity and energy can be calculated. For a more accurate comparison with the experiment, we also included the effect of the finite spatial resolution of

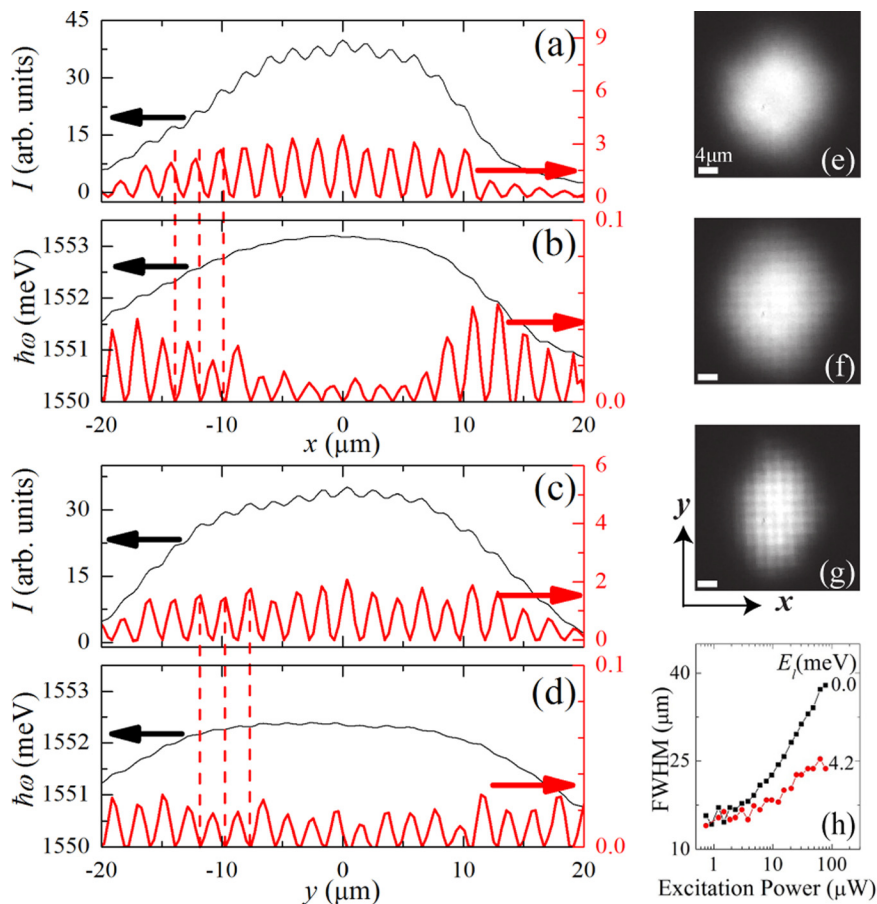


FIG. 2. (Color online) (a) PL intensity and (b) energy of excitons in a square lattice along  $x$  (black). The same data with a smooth curve subtracted (red, gray in print). (c) and (d) Similar data along  $y$ . Dashed lines are guides to the eye. Laser spot FWHM is  $17 \mu\text{m}$  along  $x$  and  $14 \mu\text{m}$  along  $y$ .  $P_{ex} = 40 \mu\text{W}$ ,  $E_l = 4.2 \text{ meV}$ . (e)–(g) Exciton PL images in a square lattice for  $P_{ex} = 11 \mu\text{W}$  at  $E_l = 0, 2.1, \text{ and } 4.2 \text{ meV}$ , respectively. (g) FWHM of exciton cloud emission along  $x$  for  $E_l = 0$  (black) and  $4.2 \text{ meV}$  (red, gray in print) vs  $P_{ex}$ .

our optical system, see supplementary information (SI).<sup>26</sup> The choice of the parameters  $T = 3.6 \text{ K}$ ,  $\zeta = 5.0 \text{ meV}$ , and  $\gamma = 2.3$  leads to a reasonable agreement between the simulations (Fig. 3) and the experiment (Fig. 2).

Concluding the paper, we comment on the Mott insulator (MI) to superfluid (S) transition. As described in SI (Ref. 26), our system can be mapped to the Bose-Hubbard model characterized by two parameters, the inter-site hopping  $J$  and the on-site interaction  $U$ . These  $J$  and  $U$  can be expressed in terms of the lattice amplitude  $E_l$  and the “recoil” energy  $E_r = \hbar^2/2mb^2$ , where  $b$  is the lattice period and  $m$  is the exciton mass. The incompressible MI state exists at  $T = 0$ . However, a finite- $T$  crossover boundary between MI and normal (N) state can be defined.<sup>24</sup> This boundary as well as the S-N transition line<sup>25</sup> are shown in Fig. 4 for the case of one particle per site,  $\bar{n} = 1$ .

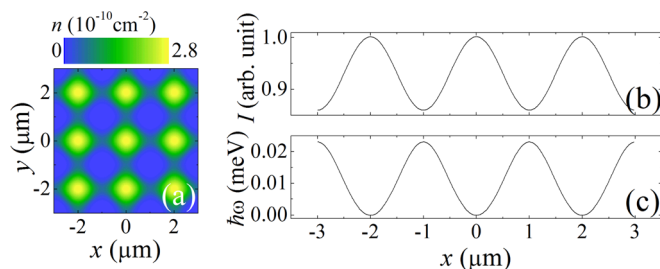


FIG. 3. (Color online) Simulations for a square lattice. (a) Exciton density. Emission (b) intensity and (c) energy with averaging in  $y$  and accounting for spatial resolution as in the experiment.  $E_l = 4.2 \text{ meV}$ ,  $\gamma = 2.3$ ,  $T = 3.6 \text{ K}$ ,  $NA = 0.245$ .

If  $T$  is fixed but  $E_l$  increases, the system traces a certain path in the phase diagram. Shown in Fig. 4 are the traces computed for  $T = 0.80, 0.35, \text{ and } 0.12 E_r$  (top to bottom). The MI-S transition is well resolved in the region somewhat below the last path, i.e., at  $T \lesssim 0.1 E_r$ , where the intervening N domain is narrow. This condition can be met for experimentally achievable parameters, e.g.,  $b \sim 200 \text{ nm}$  and  $T \lesssim 50 \text{ mK}$ . Furthermore, the conditions for observing the MI-S transition are less demanding in systems with large  $\bar{n}$ , which are similar to Josephson junction arrays (see SI). Demonstration of these transitions is a subject for future study.

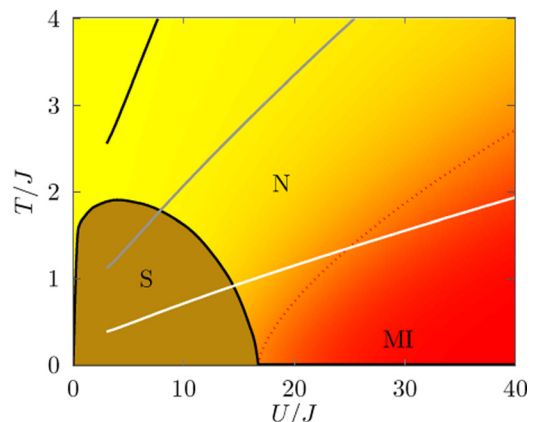


FIG. 4. (Color online) Phase diagram of the Bose-Hubbard model with one particle per site.<sup>24,25</sup>

This work is supported by the DOE Office of Basic Energy Sciences under award DE-FG02-07ER46449. M.M.F. is supported by UCOP.

- <sup>1</sup>M. Greiner, O. Mandel, T. Esslinger, T. W. Hänsch, and I. Bloch, *Nature* **415**, 39 (2002).
- <sup>2</sup>S. Zimmermann, G. Schedelbeck, A. O. Govorov, A. Wixforth, J. P. Kotthaus, M. Bichler, W. Wegscheider, and G. Abstreiter, *Appl. Phys. Lett.* **73**, 154 (1998).
- <sup>3</sup>A. T. Hammack, N. A. Gippius, S. Yang, G. O. Andreev, L. V. Butov, M. Hanson, and A. C. Gossard, *J. Appl. Phys.* **99**, 066104 (2006).
- <sup>4</sup>J. Rudolph, R. Hey, and P. V. Santos, *Phys. Rev. Lett.* **99**, 047602 (2007).
- <sup>5</sup>C. W. Lai, N. Y. Kim, S. Utsunomiya, G. Roumpos, H. Deng, M. D. Fraser, T. Byrnes, P. Recher, N. Kumada, T. Fujisawa *et al.*, *Nature* **450**, 529 (2007).
- <sup>6</sup>M. Remeika, J. C. Graves, A. T. Hammack, A. D. Meyertholen, M. M. Fogler, L. V. Butov, M. Hanson, and A. C. Gossard, *Phys. Rev. Lett.* **102**, 186803 (2009).
- <sup>7</sup>E. A. Cerda-Méndez, D. N. Krizhanovskii, M. Wouters, R. Bradley, K. Biermann, K. Guda, R. Hey, P. V. Santos, D. Sarkar, and M. S. Skolnick, *Phys. Rev. Lett.* **105**, 116402 (2010).
- <sup>8</sup>T. Byrnes, P. Recher, and Y. Yamamoto, *Phys. Rev. B* **81**, 205312 (2010).
- <sup>9</sup>H. Flayac, D. D. Solnyshkov, and G. Malpuech, *Phys. Rev. B* **83**, 045412 (2011).
- <sup>10</sup>A. G. Winbow, J. R. Leonard, M. Remeika, Y. Y. Kuznetsova, A. A. High, A. T. Hammack, L. V. Butov, J. Wilkes, A. A. Guenther, and A. L. Ivanov *et al.*, *Phys. Rev. Lett.* **106**, 196806 (2011).
- <sup>11</sup>M. Hagn, A. Zrenner, G. Böhm, and G. Weimann, *Appl. Phys. Lett.* **67**, 232 (1995).
- <sup>12</sup>T. Huber, A. Zrenner, W. Wegscheider, and M. Bichler, *Phys. Status Solidi A* **166**, R5 (1998).
- <sup>13</sup>A. Gärtner, A. W. Holleithner, J. P. Kotthaus, and D. Schul, *Appl. Phys. Lett.* **89**, 052108 (2006).
- <sup>14</sup>G. Chen, R. Rapaport, L. N. Pfeifer, K. West, P. M. Platzman, S. Simon, Z. Vörös, and D. Snoke, *Phys. Rev. B* **74**, 045309 (2006).
- <sup>15</sup>A. A. High, A. T. Hammack, L. V. Butov, M. Hanson, and A. C. Gossard, *Opt. Lett.* **32**, 2466 (2007).
- <sup>16</sup>A. A. High, E. E. Novitskaya, L. V. Butov, M. Hanson, and A. C. Gossard, *Science* **321**, 229 (2008).
- <sup>17</sup>G. Grosso, J. Graves, A. T. Hammack, A. A. High, L. V. Butov, M. Hanson, and A. C. Gossard, *Nat. Photonics* **3**, 577 (2009).
- <sup>18</sup>A. A. High, A. K. Thomas, G. Grosso, M. Remeika, A. T. Hammack, A. D. Meyertholen, M. M. Fogler, L. V. Butov, M. Hanson, and A. C. Gossard, *Phys. Rev. Lett.* **103**, 087403 (2009).
- <sup>19</sup>L. V. Butov, A. L. Ivanov, A. Imamoglu, P. B. Littlewood, A. A. Shashkin, V. T. Dolgoplov, K. L. Campman, and A. C. Gossard, *Phys. Rev. Lett.* **86**, 5608 (2001).
- <sup>20</sup>J. Krauß, J. P. Kotthaus, A. Wixforth, M. Hanson, D. C. Driscoll, A. C. Gossard, D. Schuh, and M. Bichler, *Appl. Phys. Lett.* **85**, 5830 (2004).
- <sup>21</sup>Y. Y. Kuznetsova, A. A. High, and L. V. Butov, *Appl. Phys. Lett.* **97**, 201106 (2010).
- <sup>22</sup>M. M. Dignam and J. E. Sipe, *Phys. Rev. B* **43**, 4084 (1991).
- <sup>23</sup>M. H. Szymanska and P. B. Littlewood, *Phys. Rev. B* **67**, 193305 (2003).
- <sup>24</sup>K. W. Mahmud, E. N. Duchon, Y. Kato, N. Kawashima, R. T. Scalettar, and N. Trivedi, *Phys. Rev. B* **84**, 054302 (2011).
- <sup>25</sup>B. Capogrosso-Sansone, Ş. G. Söyler, N. Prokof'ev, and B. Svistunov, *Phys. Rev. A* **77**, 015602 (2008).
- <sup>26</sup>See supplementary material at <http://dx.doi.org/10.1063/1.3682302> for the description of electrostatic potential simulations, Bose-Hubbard model parameters, and effects of optical resolution.

# Supplementary Information for “Two-Dimensional Electrostatic Lattices for Indirect Excitons”

M. Remeika, M.M. Fogler, and L.V. Butov

Department of Physics, University of California at San Diego, La Jolla, CA 92093-0319

M. Hanson and A.C. Gossard

Materials Department, University of California at Santa Barbara, Santa Barbara, California 93106-5050

(Dated: January 16, 2012)

## ELECTROSTATIC SIMULATIONS

The electrostatic potential  $\Phi(\mathbf{r})$  in the system in the absence of excitons was calculated numerically using COMSOL Multiphysics 4.0 software package. The system was modeled as a rectangular box  $1\ \mu\text{m}$  thick in the  $z$  direction and five or more lattice periods wide in the  $x$  and  $y$  directions with the electrode pattern embedded into the top surface of the box. The potential was calculated by solving the Laplace equation in the volume of the box. At the electrode surfaces the boundary condition of constant potential was imposed, e.g., at the ground plane (bottom surface) we have  $\Phi = 0$ . At all the other surfaces of the simulation box the condition of vanishing electric displacement was chosen. The  $z$ -component of the electric field at  $100\ \text{nm}$  from the bottom plane (corresponding to the location of the quantum wells) was used to calculate the potential experienced by excitons  $E(x, y) = edF_z(x, y)$ . Representative results shown in Fig. 1b in the main text, indicate that for the square-lattice case, the lattice potential can be modeled by

$$E(x, y) = E_l (\cos^2 Qx + \cos^2 Qy). \quad (1)$$

Parameters  $E_l$  and  $b = \pi/Q$  define, respectively, the amplitude and the period of  $E(x, y)$ .

The local-density approximation for the exciton density profile used in the main text is based on the assumption that  $Q$  is small enough. The necessary condition is  $E_r < E_l$ , where  $E_r$  is the “recoil” energy

$$E_r = \frac{\hbar^2 Q^2}{2m}. \quad (2)$$

In the experiments where  $E_l = 2\text{--}6\ \text{meV}$ ,  $b = 2\ \mu\text{m}$ , and the exciton mass is  $m = 0.2$  free electron mass, we have  $E_r = 0.5\ \mu\text{eV}$ , so that this condition is well satisfied.

## BOSE-HUBBARD MODEL PARAMETERS

A generic model for lattice bosons is the Bose-Hubbard model (BHM). The BHM Hamiltonian [4]

$$H = -J \sum_{\langle i,j \rangle} c_i^\dagger c_j + \frac{U}{2} \sum_i c_i^\dagger c_i (c_i^\dagger c_i - 1), \quad (3)$$

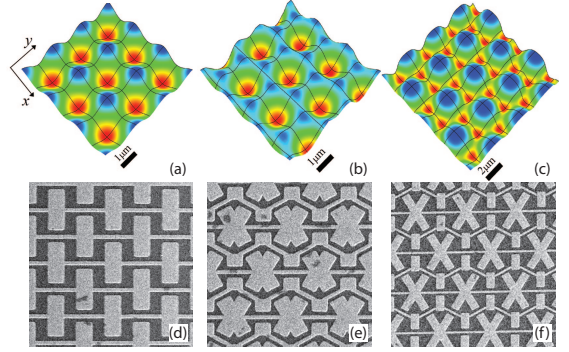


FIG. 1. (color online) (a-c) Simulated exciton energy for square, triangular, and honeycomb lattice. (d-f) SEM images of the electrode patterns.

has two parameters: the nearest-neighbor hopping  $J$  and the on-site repulsion  $U$ . The phase diagram of the BHM is well known. The ground-state of the system is either superfluid or Mott insulator. The latter is realized if the average number of bosons per site  $\bar{n}$  is an integer and the ratio  $U/J$  is large enough. The case of  $\bar{n} = 1$  is illustrated in Fig. 4 of the main text. The critical parameter ratio is [1–3]  $(U/J)_c = 16.7392$ ; at large  $\bar{n}$ , it increases according to the scaling law  $(U/J)_c \propto \bar{n}$  [4].

We can establish an approximate relation between  $J$  and  $U$  and the microscopic parameters of our exciton system as follows. Parameter  $J$  determines the single-particle bandwidth  $8J$  in the BHM. In the continuum model, the same quantity is determined by the actual band-structure of the potential  $E(x, y)$ . The lowest-energy band, relevant for the case of  $\bar{n} = 1$ , can be derived by the quasiclassical method [5], which yields

$$J \simeq \frac{4}{\sqrt{\pi}} (E_r E_l^3)^{1/4} \exp(-2\sqrt{E_l/E_r}). \quad (4)$$

Parameter  $U$  represents the interaction energy of two excitons confined to a single minimum of potential  $E(x, y)$ . For crude estimate, we replace  $E(x, y)$  by a parabolic potential well of the same curvature and treat excitons as bosons without any internal structure. The calculation is simplified by the separation of the center-of-mass and relative coordinates in the parabolic-well problem. It

leads to the following expression for the energy of two-exciton system

$$\varepsilon = \hbar\omega_0 + \Delta\varepsilon, \quad \hbar\omega_0 = 2\sqrt{E_l E_r}, \quad (5)$$

where  $\omega_0$  is the oscillator frequency in the potential well. The term  $\Delta\varepsilon$  is the ground-state energy of a particle with reduced mass  $m/2$  subject to the axially symmetric potential

$$V(r) = V_{ex}(r) + \frac{1}{4}m\omega_0^2 r^2. \quad (6)$$

It is easy to see that for a *short-range* exciton interaction potential  $V_{ex}(r)$  we have  $U < 2\hbar\omega_0$ . Indeed, for vanishing  $V_{ex}$  we get  $\Delta\varepsilon = \hbar\omega_0$  while for infinitely strong repulsion, we get  $\Delta\varepsilon = 3\hbar\omega_0$ . The actual exciton interaction potential  $V_{ex}(r)$  is close to the dipolar one  $V_{ex}(r) \propto 1/r^3$ . Solving for  $\Delta\varepsilon$  numerically, we have found that the approximation

$$U = c_1 \hbar\omega_0, \quad c_1 \approx 0.5 \quad (7)$$

holds with 30% accuracy for a wide range of experimental parameters. The weak variation of  $U$  as a function of these parameters is due to the slow logarithmic dependence of the scattering phase shift in two dimensions [6].

Using Eqs. (4) and (7), we computed the  $J$  and  $U$  as a function of  $E_l$  at three different temperatures and overlaid the resultant dependence of  $T/J$  on  $U/J$  on the BHM phase diagram [2, 3], see Fig. 4 of the main text. These calculations indicate that the observability of the Mott insulator-superfluid (MI-S) transition requires the condition

$$T \lesssim 0.1E_r \quad (8)$$

to be met. The right-hand side of this inequality depends primarily on the lattice period  $b$ . This condition can be met e.g. for  $b \sim 200$  nm and  $T \lesssim 50$  mK, showing that the MI-S transition may be realized at experimentally achievable conditions. This temperature is a factor of  $\sim 10^6$  higher than the temperature needed to observe the MI-S transition in cold atom systems where  $E_r \sim 20$  nK due to much heavier particle mass. Similarly, the superfluid-normal (SN) transition temperature for excitons is a factor of  $\sim 10^6$  higher than for the atoms.

A more practical route to realizing the MI-S transition for excitons is working with large  $\bar{n}$ . The effective Hamiltonian becomes [4]

$$H = -\frac{J_*}{2} \sum_{\langle ij \rangle} \cos(\phi_i - \phi_j) + \frac{U}{2} \sum_i n_i^2, \quad (9)$$

similar to that of Josephson junction arrays. Here the phase operator  $\phi_i$  is canonically conjugate to the occupation number  $n_i$  and  $J_* \approx J\bar{n}$ , i.e., it is much larger than  $J$ . Parameter  $J$  itself is greatly enhanced compared to Eq. (4) because the self-consistent screening of the lattice potential (see the main text) reduces the potential barrier for tunneling. As a result, the temperature range for observability of the transition can be expanded by orders of magnitude.

### OPTICAL RESOLUTION EFFECTS

The spatial resolution of the optical system is described by its point spread function (PSF)  $P(\mathbf{r})$ . We used the following common model [7] for the PSF

$$P(\mathbf{r}) = \left| \int d^2q \Theta(Q - |\mathbf{q}|) e^{i\mathbf{q}\cdot\mathbf{r} - i\delta^2 q^2/2} \right|^2. \quad (10)$$

This PSF has a finite width determined by the length scale  $Q^{-1} \equiv \lambda/(2\pi\text{NA}) = 0.46 \mu\text{m}$  set by the numerical aperture NA of the system and by another length scale  $\delta \sim 1 \mu\text{m}$  that describes defocussing. The observable intensity  $I(\mathbf{r})$  and its first spectral moment  $M_1(\mathbf{r})$  were calculated by taking the convolution of the PSF and the “ideal”  $I$  and  $M_1$  derived from the mean-field theory described in the main text.

- 
- [1] M. P. A. Fisher, P. B. Weichman, G. Grinstein, and D. S. Fisher, Phys. Rev. B **40**, 546 (1989).
  - [2] W. Krauth and N. Trivedi, Europhys. Lett. **14**, 627 (1991).
  - [3] Barabar Capogrosso-Sansone, Şebnem Güneş Söyler, Nikolay Prokof'ev, and Boris Svistunov, Phys. Rev. A **77**, 015602 (2008).
  - [4] K. W. Mahmud, E. N. Duchon, Y. Kato, N. Kawashima, R. T. Scalettar, and N. Trivedi, Phys. Rev. B **84**, 054302 (2011).
  - [5] H. Neuberger, Phys. Rev. D **17**, 498 (1977).
  - [6] A. D. Meyertholen and M. M. Fogler, Phys. Rev. B. **78**, 235307 (2008).
  - [7] H. H. Hopkins, Proc. Roy. Soc. London Ser. A **231**, 91 (1955).

Copyright 2012 American Institute of Physics. This article may be downloaded for personal use only. Any other use requires prior permission of the author and the American Institute of Physics.

The following article appeared in Appl. Phys. Lett. 100, 061103 and may be found at <http://link.aip.org/link/?APL/100/061103>.